Heterogeneity of foam cell biogenesis across diseases

Valentina Guerrini [1*], Brendan Prideaux [4], Rehan Khan [1], Selvakumar Subbian [1,2], Yina Wang [1], Evita Sadimin [5*], Siddhi Pawar [1], Rahul Ukey [1], Eric A. Singer [6*], Chaoyang Xue [1,3], Maria Laura Gennaro [1,2**]

[1] Public Health Research Institute, [2] Department of Medicine, and [3] Department of Microbiology, Rutgers New Jersey Medical School, Rutgers Biomedical and Health Sciences, Newark, NJ 07103

[4] Department of Neurobiology, University of Texas Medical Branch, Galveston, TX 77555

[5] Section of Urologic Pathology and [6] Section of Urologic Oncology, Rutgers Cancer Institute of New Jersey and Rutgers Robert Wood Johnson Medical School, New Brunswick, NJ 08901

***Current addresses:** Boehringer Ingelheim Animal Health, Ames, IA 50010 (VG); City of Hope National Medical Center, Duarte, CA 91010 (ES); Division of Urologic Oncology, The Ohio State University Comprehensive Cancer Center, Columbus, OH 43221 (EAS).

****Corresponding author:** marila.gennaro@rutgers.edu

Classification: Biological sciences; Cell biology

Keywords: kidney disease; tuberculosis; cryptococcosis; papillary renal cell carcinoma; lipid metabolism; storage lipids

Abbreviations: CE, cholesteryl esters; H&E, hematoxylin and eosin; MALDI, matrix-assisted laser desorption/ionization mass spectrometry; MDM, monocyte-derived macrophages; pRCC, papillary renal cell carcinoma; TAG, triglycerides.

Significance statement. Chronic inflammatory states of infectious and non-infectious etiology are associated with dysfunctional immune responses. Primary contributors are foam cells, lipid-laden macrophages exhibiting impaired or pathogenic immune functions. In contrast with the long-standing paradigm derived from atherosclerosis, a disease in which foam cells are cholesterol-laden, our work demonstrates that foam cells are heterogeneous. Utilizing bacterial, fungal, and cancer models, we show that foam cells may accumulate various storage lipids (triglycerides and/or cholesteryl esters) by mechanisms that depend on disease-specific microenvironments. Thus, we present a new framework for foam cell biogenesis in which the atherosclerosis paradigm represents only a specific case. Since foam cells are potential therapeutic targets, understanding their mechanisms of biogenesis will provide knowledge needed for novel therapeutic approaches.

Abstract. Foam cells are dysfunctional, lipid-laden macrophages associated with chronic inflammation of infectious and non-infectious origin. For decades, the paradigm underlying foam cell biology has been based on atherogenesis, a disease in which macrophages are cholesterol-enriched. Our previous work showed that foam cells in tuberculous lung lesions surprisingly accumulate triglycerides, suggesting multiple modalities of foam cell biogenesis. In the present study, we used matrix-assisted laser desorption/ionization mass spectrometry imaging to assess the spatial distribution of storage lipids relative to foam-cell-rich areas in murine lungs infected with the fungal pathogen *Cryptococcus neoformans* and in human papillary renal cell carcinoma resection tissues. We also analyzed neutral lipid content and the transcriptional program of lipid-laden macrophages generated under corresponding in vitro conditions. The in vivo data were consistent with in vitro findings showing that *C. neoformans*-infected macrophages accumulated triglycerides, while macrophages exposed to human renal cell carcinoma-conditioned medium accumulated both triglycerides and cholesterol. Moreover, macrophage transcriptome analyses provided evidence for condition-specific metabolic remodeling. The in vitro data also showed that although both *Mycobacterium tuberculosis* and *C. neoformans* infections induced triglyceride accumulation in macrophages, they did so by different molecular mechanisms, as evidenced by different sensitivity of lipid accumulation to the drug rapamycin and the characteristics of macrophage transcriptome remodeling. Collectively, these data demonstrate that the mechanisms of foam cell formation are specific to the disease microenvironment. Since foam cells have been regarded as targets of pharmacological intervention in several diseases, recognizing that their formation is disease-specific opens new research directions of biomedical significance.

Chronic inflammation of infectious and non-infectious origin is often associated with the presence of foam cells, lipid-laden macrophages that exhibit impaired immune function and can contribute to pathogenesis (1). Foam cells form when, due to dysregulated metabolism, lipids accumulate beyond the homeostatic capacity of macrophages. The lipids are stored as droplets that confer a foamy appearance to the macrophages (2). Our understanding of foam cell biology has been largely based on studies of atherogenesis, a disease in which uptake of normal and proinflammatory lipoproteins by macrophages in the arterial wall leads to imbalanced cholesterol metabolism and formation of cholesterol-laden foam cells (3). The accumulation of foam cells in the arterial intima leads to chronic inflammation, cell death, and tissue necrosis (3). A similar situation is observed in tuberculosis, a chronic inflammatory disease of the lung caused by *Mycobacterium tuberculosis*. In the tuberculous lung lesions, which are called granulomas, the presence of tissue necrosis is associated with foam cell accumulation (1). Indeed, foam cells are a hallmark of both the atherosclerotic plaque and the necrotizing tuberculous granuloma (3, 4). We were surprised to find that the foam cells of necrotic tuberculous lung lesions are enriched in triglycerides (TAG) (5). Work with cultured human macrophages and mice further established that *M. tuberculosis* infection induces TAG accumulation in macrophages (5, 6). Thus, the atherosclerosis and tuberculosis models of foam cells are fundamentally different, indicating that foam cells may form via different mechanisms in different diseases.

To test the hypothesis that foam cell biogenesis is disease-specific, we began a study of foam cells resulting from another infectious disease, cryptococcosis, and from a form of cancer. Cryptococcosis is a clinically heterogeneous disease caused by the fungal pathogen *Cryptococcus neoformans*. It affects the lung and other organ systems, including the central nervous system, particularly in immunocompromised individuals (7). Foam cells have been observed in human tissue biopsies from pulmonary and extrapulmonary cryptococcosis (8, 9) and in the lungs of infected mice (10). Foam cells have also been associated with several forms of cancer of many organ systems that include liver, lung, colon/rectum, and kidney (11-14). Indeed, the presence of foam cells is a histological feature of papillary renal cell carcinoma (pRCC) (15, 16). Factors released by cultured pRCC cells induce lipid accumulation in macrophages (13), indicating that the microenvironment of this tumor is lipogenic for macrophages. The nature of storage lipids and the mechanism of foam cell formation are poorly understood in these pathologies.

98 In the present work, we assessed the spatial distribution of foam cells and storage lipids in *C.*
99 *neoformans*-infected murine lungs and in human pRCC specimens. We then analyzed lipid
100 content and the transcriptional program of lipid-laden macrophages generated under in vitro
101 conditions that corresponded to these two diseases. The data established that the mechanism
102 underlying foam cell formation varies with disease context. We can no longer base our
103 understanding of foam cell biogenesis only on work focused on atherogenesis. Expanding our
104 view of foam cell biogenesis may provide new targets for therapeutic intervention into diseases -
105 - such as atherosclerosis, tuberculosis, multiple sclerosis, and certain cancers -- in which foam
106 cell appearance and poor clinical outcome are associated (reviewed in (1)).

107

108 **Materials and Methods.** The supplementary materials include the description of the materials
109 and methods utilized to generate, culture, infect and/or treat human monocyte-derived
110 macrophages; to perform cell culture processing and measurements of released cytokines and
111 chemokines; neutral lipid content; RNA extraction and bulk RNA sequencing with the associated
112 statistical analyses; to conduct mouse infections with *C. neoformans*; to obtain and process
113 cryptococcus-infected murine lungs and human cancerous kidney specimens for histopathology
114 and analysis of spatial distribution of cholesteryl esters and triglycerides by matrix-assisted laser
115 desorption/ionization mass spectrometry.

116

117 **Results**

118 **Foam cells cluster peri- or extra-lesionally and associate with TAG species in *C.***
119 ***neoformans*-infected murine lungs.**

120 Foam cells form during pulmonary and extrapulmonary cryptococcal infection (8, 9). We used a
121 model of pulmonary cryptococcosis in C57BL/6 mice to assess the spatial relationship between
122 foam cells and neutral lipids [TAG and cholesteryl esters (CE)] in infected lungs. At 7 days post
123 intranasal infection, infected mouse lungs exhibited several granulomatous nodular lesions
124 visible at low magnification (**Fig. S1**). The lesions consisted of large aggregates of fungal cells
125 surrounded by inflammatory infiltrates comprised mostly of polymorphonuclear cells,
126 macrophages and lymphocyte aggregates, and epithelioid cells (**Fig. 1A**). Foam cells tended to
127 form clusters in peri- or extra-lesional areas of the infected foci in the lungs [hematoxylin and

128 eosin (H&E)-stained lung slices in **Fig. 1BC**]. When we used matrix-assisted laser
129 desorption/ionization mass spectrometry (MALDI) imaging of sections adjacent to those used for
130 H&E staining, we detected multiple TAG and CE species in the infected lungs (**Table S1**). All
131 CE species localized in the fungus-rich lesions (e.g., compare H&E staining and MALDI imaging
132 for CE 16:0 in **Fig. 1C**). In contrast, TAG species were distributed throughout the lung tissue,
133 with some species, such as TAG 46:0, more prominently found within the lesions and others,
134 such as TAG 50:1, found extra-lesionally (**Fig. 1C,** with corresponding ion counts in **Fig. 1D**)
135 (see **Fig. S2** for uninfected control tissue). Localization of some TAG species and CE species in
136 the fungus-rich lesions is consistent with the presence of TAG and sterols in fungal cells (17,
137 18). In addition, the spatial distribution of some TAG species, such as TAG 50:1 in **Fig. 1C**,
138 which was present throughout the tissue but approximately two-fold lower in the fungus-rich
139 lesions, corresponds to that of foam cells (compare H&E staining and MALDI imaging in **Fig.**
140 **1C**), suggesting that *Cryptococcus*-induced foam cells are TAG enriched.

141 ***Cryptococcus neoformans* infection induces accumulation of TAG-rich lipid droplets in**
142 **macrophages via an mTORC1-independent pathway.**

143 MALDI imaging provides information about the spatial distribution of analytes in tissues, but it
144 does not have the single-cell resolution needed to precisely assign a particular neutral lipid to a
145 specific cell type. Thus, we utilized an in vitro infection model to study neutral lipid accumulation
146 in macrophages infected with *C. neoformans*. We infected primary human monocyte-derived
147 macrophages (MDM) with mCherry-expressing *C. neoformans* H99, quantified lipid droplet
148 content by imaging flow cytometry, and observed a significant lipid droplet accumulation in
149 infected macrophages (3.5-fold increase relative to uninfected cells) (**Fig. 2AB**). Lipid-droplet-
150 enriched macrophages in the infected culture wells included both those containing fungal cells
151 and those that did not (**Fig. 2A** and quantitative data in **Fig. S3A**). These data indicated that
152 lipid droplet formation does not require internalization of fungal cells. Since lipid droplets
153 accumulated in macrophages exposed to cell-free *C. neoformans* culture filtrate (**Fig. S3B**) but
154 not in macrophages exposed to heat-killed fungi (**Fig. S3C**), lipid droplet accumulation in
155 macrophages appears to involve a factor(s) released from live *C. neoformans* cells.

156 When we measured storage lipid content in *C. neoformans*-infected cells by an enzymatic
157 assay, we found that infection increased the content of intracellular TAG but not cholesterol
158 derivatives (**Fig. 2C**). Moreover, lipid droplet accumulation in *C. neoformans*-infected cells was
159 essentially abrogated by treatment with an inhibitor of diglyceride acetyl transferase

(A9222500), the enzyme that catalyzes the conversion of di- to tri-glycerides (**Fig. 2D**). This finding supports the conclusion that *C. neoformans*-induced lipid droplets are TAG enriched, as previously seen with *M. tuberculosis* infection ((5) and **Fig. 2D**).

Our previous work showed that the accumulation of TAG-rich lipid droplets in macrophages infected with *M. tuberculosis* requires mTORC1 signaling, as it is inhibited by rapamycin treatment (5). Unlike the *M. tuberculosis* case, however, rapamycin had no effect on lipid droplet accumulation in *C. neoformans*-infected macrophages (**Fig. 2D**). Thus, even though *M. tuberculosis* and *C. neoformans* both induce accumulation of TAG-rich lipid droplets, the two pathogens do so by utilizing different signaling mechanisms.

Transcriptomics identify different molecular mechanisms of TAG accumulation in *M. tuberculosis*- and *C. neoformans*-infected macrophages.

We investigated the pathways underlying TAG accumulation in *M. tuberculosis*- and *C. neoformans*- infected macrophages by conducting transcriptomics analyses of macrophages obtained from the same donors and infected in vitro with either pathogen. When we analyzed the Gene Ontology (GO) annotations related to metabolic processes, we found that the most informative signatures of macrophage metabolic reprogramming associated with TAG accumulation derived from the downregulated pathways in *M. tuberculosis*-infected macrophages and from the upregulated pathways in *C. neoformans*-infected macrophages. The former included lipid catabolism, fatty acid oxidation, oxidative phosphorylation, and electron transport chain (**Fig. 2E**), while the latter were enriched for glycolysis (**Fig. 2F**).

Metabolism-related analyses at the gene level (**Table S2** and *Supplementary text*) showed that, in *M. tuberculosis*-infected macrophages, the top three downregulated metabolic genes encoded: (i) acyl-CoA synthase (ACSM5), (ii) carnitine octanoyl transferase (CROT), which converts acyl-CoA to acyl-carnitine, a step required for transport across the mitochondrial membrane, and iii) aldehyde hydrogenase (ALDH3A2), which oxidizes fatty aldehydes to fatty acids. Downregulation of these genes likely leads to defective fatty acid oxidation. In *C. neoformans* infection, the top five upregulated metabolic genes all encoded glycolytic enzymes (**Table S3** and *Supplementary text*). We also found indicators of reduced mitochondrial functions in *C. neoformans*-infected macrophages, including downregulation of polyribonucleotide nucleotidyl transferase 1 (PNPT1) and a glutaminyl-tRNA amidotransferase subunit 1 (QRSL1) (**Table S3**). The PNTP1 product regulates mitochondrial homeostasis and

the abundance of electron transport chain components (19). Missense mutations in the human QRSL1 locus have been associated with defects in oxidative phosphorylation (20). In addition, several aldehyde dehydrogenases were downregulated in *C. neoformans*-infected macrophages, an indicator of reduced fatty acid oxidation (**Table S3** and *Supplementary text*).

We identified additional gene expression markers of TAG accumulation in the two infections. For example, in *M. tuberculosis* infection, we observed downregulation of lipolytic genes, upregulation of sirtuins and sirtuin-stabilizing functions, and expression changes in genes signifying increased production of ceramide and altered cellular redox. These can all lead to TAG accumulation (see **Table S2** and *Supplementary text*). In *C. neoformans* infection, additional indicators of metabolic remodeling toward TAG biosynthesis included (i) upregulation of genes for the production of dihydroxyacetone phosphate, which can be routed toward TAG biosynthesis, (ii) upregulation of hexokinase (HK2) and lactate dehydrogenase (LDHA), which indirectly inhibit lipolysis, and (iii) downregulation of AMP-activated protein kinase (AMPK), which inhibits de novo biosynthesis of fatty acids and stimulates fatty acid oxidation (21) (see **Table S3**). These and additional markers of lipid accumulation are discussed further in the *Supplementary text*.

The transcriptomics data also shed light on the requirement in *M. tuberculosis* infection for signaling by mechanistic target of rapamycin complex 1 (mTORC1) (**Fig. 2D**), which is lipogenic in multiple ways (22). *M. tuberculosis*-infected macrophages showed downregulated TP53 gene and upregulated TP53-specific E3 ligases that target this factor for proteasomal degradation (see **Table S2** and *Supplementary text*). Decreased activity of TP53 correlates well with increased mTORC1 signaling, since TP53 induces expression of Deptor (**Table S2**) and leads to activation of AMPK, two factors that inhibit mTORC1 (23, 24).

We conclude that, with both infections, the accumulation of TAG results from decreased oxidative phosphorylation, increased glycolysis, increased lipid biosynthesis, and decreased lipid catabolism. However, the molecular modalities of macrophage metabolic reprogramming differ between the two infections.

Cytokine profiles differ between *C. neoformans*- and *M. tuberculosis*-infected macrophages.

Key elements of macrophage phenotypes are the cytokines and chemokines they produce when stimulated. Cytokine/chemokine production may be relevant to lipid metabolism

dysregulation since, for example, lipid droplet accumulation in *M. tuberculosis*-infected macrophages requires signaling through the receptor for TNFα, a proinflammatory cytokine involved in lipid homeostasis (5). Indeed, treating with TNFα induces lipid droplet accumulation in human macrophages (**Fig. S5**). Thus, autocrine/paracrine mechanisms may be at play in lipid droplet formation. When we tested for the production of selected cytokines/chemokines during *C. neoformans* infection, we found no quantitative differences for 43 cytokines and chemokines in the culture media of non-infected vs. infected macrophages (**Fig. 2G** and not shown). In contrast, in response to *M. tuberculosis* infection, macrophages produced many cytokines and chemokines that were mostly proinflammatory (**Fig. 2G**). Thus, at least in vitro, the cytokine/chemokine milieu of macrophages infected with *C. neoformans* and *M. tuberculosis* differed greatly. That difference may contribute to the different mechanisms of lipid accumulation seen in the two infections.

Foam cells preferentially associate with CE- and TAG-enriched kidney areas in papillary renal cell carcinoma.

Papillary renal cell carcinoma (pRCC) is useful for studies of foam cell biogenesis in a cancer context, since foam cells are a frequent histopathologic finding in this type of cancer (15, 16). To characterize pRCC-associated foam cells, we used pRCC specimens obtained from patients who underwent partial or radical nephrectomy and performed MALDI imaging and H&E staining of adjacent sections of the resected tissues. Nine CE species were detected in the pRCC tissues. Most were distributed throughout the tissue, but their localization varied with the degree of saturation of the esterified fatty acid (**Fig. S6**, **Table S1**). In particular, the two monounsaturated species (CE 16:1 and CE 18:1), which were the most abundant in the tissues, associated with highly localized, intense signals (CE 16:1 tissue localization is shown in **Fig. 3A**). In contrast, TAG species yielded only localized signals, which were similar for all detected TAGs (**Fig. 3B** shows the distribution of TAG 52:2, which is representative of all TAG species; see **Fig. S7** for other TAG species). H&E staining revealed that the intense localized CE signals corresponded to large foam cell aggregates (**Fig. 3CEG** show one such area at increasing magnification), while the TAG signals corresponded to tissue regions containing large numbers of foam cells interspersed among cancer cells (**Fig. 3DFH** show a representative area at increasing magnification). Given that CE species were detected throughout the tissue (**Fig. S6**), the TAG-rich regions also contained CE, albeit at lower levels than the large foam cell aggregates shown in the left panels of Fig. 3. In summary, MALDI imaging showed associations

254 between foam-rich areas with TAG species, CE species, or both, suggesting that, in pRCC,
255 foam cells may accumulate either or both classes of these storage lipids.

256 **Factor(s) released by a papillary renal cell carcinoma-like cell line induce macrophage**
257 **accumulation of both TAG and CE.**

258 We next investigated the effects of pRCC on storage lipid accumulation in macrophages in vitro
259 by exposing human macrophages to cell-free conditioned medium from cultures of the ACHN
260 cell line, which is derived from a human renal cell carcinoma and exhibits pRCC features (25).
261 Exposure to ACHN-conditioned medium induced macrophage production of chemokines and
262 cytokines, including IL-8, IL-6, CCL2, and CXCL16 (**Fig. S8A**), which are characteristic of the
263 response of tumor-associated macrophages to factors released by cancer cells (26-28). ACHN-
264 medium-treated macrophages also exhibited lipid droplet accumulation (**Fig. 4AB**), in
265 agreement with previous observations (13), indicating the presence in the medium of lipogenic
266 bioproduct(s) of the ACHN cells. Since IL-8 produced by cultured pRCC cells has been
267 proposed as a foam-cell-inducing factor (13), we investigated the relationship among pRCC,
268 foam cell formation, and IL-8 in our experimental system. We found that IL-8 is lipogenic for
269 macrophages, but at a concentration ~10-fold higher than that measured in the ACHN-
270 conditioned medium (~0.5ng/ml) (**Fig. S8BC** and **Table S4**). Moreover, blocking IL-8 activity
271 with neutralizing antibodies did not prevent lipid droplet formation in macrophages exposed to
272 ACHN medium, and IL-8 depletion from the ACHN medium had no effect on lipid droplet
273 formation (**Fig. S8D-F**). Thus, the lipogenic effect of the ACHN medium cannot be ascribed to
274 IL-8. We cannot exclude, however, that IL-8 is lipogenic via paracrine-autocrine mechanisms in
275 the tumor microenvironment in vivo since, for example, ACHN-medium-treated macrophages
276 produce lipogenic concentrations of this cytokine (~5ng/ml) (**Fig. S8A and Table S4**).

277 Storage lipid analysis by enzymatic assays showed that lipid droplet accumulation in ACHN-
278 medium-treated macrophages correlated with increased levels of TAG and cholesterol (**Fig.**
279 **4C**), suggesting yet another context-specific mechanism of foam cell formation. Indeed,
280 metabolism-related gene expression analysis identified mechanisms for both TAG and
281 cholesterol accumulation. Pathways related to glycolysis featured among the top ranked Gene
282 Ontology (GO) annotations related to metabolic processes (**Fig. 4D**). At the gene-level, the top
283 four upregulated metabolic genes encoded glycolytic enzymes (**Fig. 4D, Table S5,** and
284 *Supplementary text*). We also found gene markers of reduced TCA cycle, including upregulation
285 of adenylate kinase 4 (AK4) (**Fig. 4D**), a key metabolic regulator increasing glycolysis and

inhibiting TCA cycle and oxidative phosphorylation (29), and downregulation of PPARGC1A (**Table S5**). The latter gene encodes PGC-1α, a master regulator of energy metabolism that promotes fatty acid oxidation and TCA cycle and decreases TAG storage (30) (**Table S5** and *Supplementary text*). Together, increased glycolysis and reduced TCA cycle would result in routing of pyruvate towards de novo lipogenesis.

Among additional markers of TAG accumulation is notable the increased expression of genes associated with or regulated by YAP/TAZ signaling, which regulates metastasis and metabolic reprogramming, including lipid metabolism, in cancer cells (31). These genes include TEAD transcription factors, the perilipin PLIN5, and the fructose transporter SLC2A5 (increased fructose uptake may lead to lipogenesis via fructolysis) (**Table S5** and *Supplementary text*). Increased YAP/TAZ signaling is also supported by the above-mentioned upregulation of AK4 (**Fig. 4D**) and downregulation of phospholipase D family member 6 (PLD6) (**Table S5**), since both gene expression changes might result in decreased activity of AMPK, which inhibits YAP/TAZ (32) (**Table S5** and *Supplementary text*). Gene expression markers of impaired fatty acid oxidation and additional mechanisms of lipid accumulation in ACHN-medium-treated macrophages are discussed in the *Supplementary text*.

The ACHN-medium-treated macrophages also exhibited gene expression changes associated with dysregulation of cholesterol metabolism. For example, the scavenger receptor CD36, which is a key regulator of cholesterol homeostasis, was downregulated, presumably as a consequence of PPARGC1A downregulation (30) (**Table S5**). CD36 induces cholesterol depletion by promoting macrophage cholesterol efflux and proteasomal degradation of HMG-CoA reductase, the rate-limiting enzyme in sterol synthesis (33). An additional marker of dysregulated cholesterol homeostasis is the downregulation of adenylate cyclase (ADCY1), which generates cAMP signaling for cholesterol efflux in atherogenic foam cells (34). The above-proposed increased YAP/TAZ signaling might also result in cholesterol accumulation, since YAP/TAZ is involved in the metabolism of fatty acids and sterols (31).

Collectively, gene expression data point toward macrophage metabolic reprogramming in response to factors in the ACHN-conditioned medium. This reprogramming includes increased glycolysis, impaired TCA cycle and oxidative metabolism, decreased lipolysis, and dysregulated cholesterol homeostasis.

Discussion

The data reported above show that the mechanisms of foam cell biogenesis differ with disease context. That is the case regardless of the chemical nature of the storage lipids they accumulate. For example, macrophages infected with *M. tuberculosis* and *C. neoformans* are enriched in TAG, as demonstrated by the drastic lipid droplet decrease caused by pharmacological inhibition of TAG biosynthesis in the two infections. In both cases, the accumulation of TAG likely results from a switch from oxidative to glycolytic metabolism that includes increased biosynthesis and decreased catabolism of lipids. However, the molecular mechanisms underlying the metabolic reprogramming of macrophages differ between the two infections, as indicated by the different effect of rapamycin on lipid droplet accumulation in the two infections. Still other mechanisms are likely at play in pRCC-associated macrophages, which accumulate neutral lipids by reprogramming both cholesterol and TAG metabolism. Moreover, although gene expression levels do not directly translate into protein levels, protein activity, and metabolic fluxes, the gene expression data presented above clearly imply that the metabolic remodeling leading to neutral lipid accumulation occurs through signaling, regulatory, and effector mechanisms that are specific to each experimental condition. Therefore, our data show that macrophage foam cells in different diseases are mechanistically heterogeneous even though they may be similar histochemically (lipid droplets consistently confer a “pale bubbly” appearance upon H&E staining) and perhaps even functionally, as discussed below.

A key to understanding foam cell heterogeneity is the biochemical diversity of the microenvironments driving their biogenesis. It is well established that uptake of exogenous lipids can drive foam cell formation. This is the case in atherogenesis, where sequestration of cholesterol-rich lipoproteins in the arterial wall leads to endothelial activation, recruitment of monocytes, and monocyte differentiation into lipoprotein-ingesting phagocytes that become foam cells (3). Moreover, in some cancers, such as colon cancer, the fatty acid-enriched environment induces lipid droplet accumulation in tumor-associated macrophages (14). It would be fallacious, however, to associate foam cell formation exclusively with exogenous lipid uptake. Instead, our work points to additional scenarios in which various microenvironment-specific signals trigger a metabolic remodeling of local macrophages that leads to excess intracellular fatty acids that are detoxified by storage in droplets. These environmental triggers may include pathogen-derived molecules, cancer cell products, inflammatory signals from activated and/or damaged cells that, for example, activate Toll-like receptors (TLR) (or other pattern recognition

350 receptors) resulting in the reshaping of the macrophage lipidome (35). Additional heterogeneity
351 may result from the combinatorial effects of multiple foam-cell-inducing signals in some
352 microenvironments. For example, foam cells may be induced in pRCC by yet unidentified
353 cancer cell products, as indicated by our results with ACHN-conditioned medium, together with
354 lipogenic proinflammatory cytokines, such as IL-8, produced by tumor-associated-macrophages.
355 Moreover, additional mediators might be produced by cell types that are not represented in our
356 in vitro system, such as the lipid-filled tumor cells that we observed in the pRCC bioptic tissue.
357 In tuberculosis, we showed that, in addition to bacterial components that presumably trigger
358 TLR2 signaling (36, 37), macrophage lipid accumulation requires another lipogenic
359 proinflammatory cytokine, TNFα, produced by infected macrophages (5). Additional work is
360 needed to identify the exogenous (i.e., generated by microbes, cancer cells, or other cell types)
361 trigger signals and to determine how commonly foam cells are induced by combinations of
362 exogenous and autocrine/paracrine signals.

363 It is reasonable to assume that, despite the different mechanisms of biogenesis, the presence of
364 foam cells represents a maladaptive immune response in all the pathological contexts they
365 form. Generally, lipid-laden macrophages tend to lose protective immune functions, including
366 phagocytosis, efferocytosis, and autophagy. They can also induce tissue damage, contribute to
367 necrosis, exhibit impaired antimicrobial activity, and even sustain survival of intracellular
368 pathogens (reviewed in (1)). Indeed, given their contribution to pathogenesis, foam cells have
369 been recognized as targets of pharmacological intervention, for example in atherosclerosis and
370 some cancers (14, 38). Moreover, foam cells are often associated with kidney disease, such as
371 focal and segmental glomerulosclerosis and diabetic nephropathy (39), in addition to the pRCC
372 investigated in the present work. Their pathophysiological significance in the kidney remains
373 puzzling, and all mechanistic hypotheses on their biogenesis derive from the atherosclerosis
374 literature (39). Recognizing that foam cells do not result only from macrophage uptake of
375 exogenous lipids and that the mechanisms of their formation are microenvironment-specific
376 opens new directions for mechanistic and drug development research of high biomedical
377 significance.

378 *Acknowledgements*. We thank Knowledge Synthesis, Inc. for help with statistical analyses of the
379 transcriptomics data; Karl Drlica for critical reading of the manuscript. This work was funded by
380 NIH grants R01 HL149450, R01 HL149450-S1, R01 AI158911 (M.L.G.), R01AI155647,
381 R01AI169769 (C.X.), P30CA072720 (E.S and E.A.S), and a Cancer Prevention and Research
382 Institute of Texas (CPRIT) High Impact High Risk grant RP190669 (B.P).

References

1. V. Guerrini, M. L. Gennaro, Foam Cells: One Size Doesn't Fit All. *Trends Immunol* **40**, 1163-1179 (2019).
2. M. H. den Brok, T. K. Raaijmakers, E. Collado-Camps, G. J. Adema, Lipid Droplets as Immune Modulators in Myeloid Cells. *Trends Immunol* **39**, 380-392 (2018).
3. K. J. Moore, F. J. Sheedy, E. A. Fisher, Macrophages in atherosclerosis: a dynamic balance. *Nat Rev Immunol* **13**, 709-721 (2013).
4. D. G. Russell, P. J. Cardona, M. J. Kim, S. Allain, F. Altare, Foamy macrophages and the progression of the human tuberculosis granuloma. *Nat Immunol* **10**, 943-948 (2009).
5. V. Guerrini *et al.*, Storage lipid studies in tuberculosis reveal that foam cell biogenesis is disease-specific. *PLoS Pathog* **14**, e1007223 (2018).
6. S. Dawa *et al.*, Inhibition of Granuloma Triglyceride Synthesis Imparts Control of Mycobacterium tuberculosis Through Curtailed Inflammatory Responses. *Front Immunol* **12**, 722735 (2021).
7. E. K. Maziarz, J. R. Perfect, Cryptococcosis. *Infect Dis Clin North Am* **30**, 179-206 (2016).
8. P. Karmakar, R. Jeyarajah, V. Ramasubramanian, Isolated cryptococcal osteomyelitis in immunocompetent patient. *J Indian Med Assoc* **109**, 592, 594 (2011).
9. C. S. Thornton, O. Larios, J. Grossman, T. P. Griener, S. Vaughan, Pulmonary Cryptococcus infections as a manifestation of idiopathic CD4 lymphocytopenia: case report and literature review. *BMC Infect Dis* **19**, 862 (2019).
10. T. G. Normile, A. M. Bryan, M. Del Poeta, Animal Models of Cryptococcus neoformans in Identifying Immune Parameters Associated With Primary Infection and Reactivation of Latent Infection. *Front Immunol* **11**, 581750 (2020).
11. M. Donadon *et al.*, Macrophage morphology correlates with single-cell diversity and prognosis in colorectal liver metastasis. *J Exp Med* **217** (2020).
12. X. Liu-Jarin *et al.*, Histologic assessment of non-small cell lung carcinoma after neoadjuvant therapy. *Mod Pathol* **16**, 1102-1108 (2003).
13. K. M. Krawczyk *et al.*, Papillary renal cell carcinoma-derived chemerin, IL-8, and CXCL16 promote monocyte recruitment and differentiation into foam-cell macrophages. *Lab Invest* **97**, 1296-1305 (2017).
14. H. Wu *et al.*, Lipid droplet-dependent fatty acid metabolism controls the immune suppressive phenotype of tumor-associated macrophages. *EMBO Mol Med* **11**, e10698 (2019).

15. T. Onishi, Y. Ohishi, H. Goto, M. Suzuki, Y. Miyazawa, Papillary renal cell carcinoma: clinicopathological characteristics and evaluation of prognosis in 42 patients. *BJU Int* **83**, 937-943 (1999).
16. B. Delahunt, J. N. Eble, Papillary renal cell carcinoma: a clinicopathologic and immunohistochemical study of 105 tumors. *Mod Pathol* **10**, 537-544 (1997).
17. C. Chrissian *et al.*, Solid-state NMR spectroscopy identifies three classes of lipids in Cryptococcus neoformans melanized cell walls and whole fungal cells. *J Biol Chem* **295**, 15083-15096 (2020).
18. A. Singh, A. MacKenzie, G. Girnun, M. Del Poeta, Analysis of sphingolipids, sterols, and phospholipids in human pathogenic Cryptococcus strains. *J Lipid Res* **58**, 2017-2036 (2017).
19. G. Wang *et al.*, PNPASE regulates RNA import into mitochondria. *Cell* **142**, 456-467 (2010).
20. M. Kohda *et al.*, A Comprehensive Genomic Analysis Reveals the Genetic Landscape of Mitochondrial Respiratory Chain Complex Deficiencies. *PLoS Genet* **12**, e1005679 (2016).
21. M. Foretz, P. C. Even, B. Viollet, AMPK Activation Reduces Hepatic Lipid Content by Increasing Fat Oxidation In Vivo. *Int J Mol Sci* **19** (2018).
22. G. A. Soliman, The integral role of mTOR in lipid metabolism. *Cell Cycle* **10**, 861-862 (2011).
23. H. Chen *et al.*, DEP domain-containing mTOR-interacting protein suppresses lipogenesis and ameliorates hepatic steatosis and acute-on-chronic liver injury in alcoholic liver disease. *Hepatology* **68**, 496-514 (2018).
24. Z. Feng, H. Zhang, A. J. Levine, S. Jin, The coordinate regulation of the p53 and mTOR pathways in cells. *Proc Natl Acad Sci U S A* **102**, 8204-8209 (2005).
25. R. Sinha *et al.*, Analysis of renal cancer cell lines from two major resources enables genomics-guided cell line selection. *Nat Commun* **8**, 15165 (2017).
26. S. W. Cho *et al.*, CXCL16 signaling mediated macrophage effects on tumor invasion of papillary thyroid carcinoma. *Endocr Relat Cancer* **23**, 113-124 (2016).
27. H. Xu *et al.*, Tumor-associated macrophage-derived IL-6 and IL-8 enhance invasive activity of LoVo cells induced by PRL-3 in a KCNN4 channel-dependent manner. *BMC Cancer* **14**, 330 (2014).

28. D. Li *et al.*, Tumor-associated macrophages secrete CC-chemokine ligand 2 and induce tamoxifen resistance by activating PI3K/Akt/mTOR in breast cancer. *Cancer Sci* **111**, 47-58 (2020).
29. K. Fujisawa *et al.*, Modulation of anti-cancer drug sensitivity through the regulation of mitochondrial activity by adenylate kinase 4. *Journal of Experimental & Clinical Cancer Research* **35**, 48 (2016).
30. C. F. Cheng, H. C. Ku, H. Lin, PGC-1α as a Pivotal Factor in Lipid and Metabolic Regulation. *Int J Mol Sci* **19** (2018).
31. H. Yamaguchi, G. M. Taouk, A Potential Role of YAP/TAZ in the Interplay Between Metastasis and Metabolic Alterations. *Front Oncol* **10**, 928 (2020).
32. J. S. Mo *et al.*, Cellular energy stress induces AMPK-mediated regulation of YAP and the Hippo pathway. *Nat Cell Biol* **17**, 500-510 (2015).
33. A. Rodrigue-Way *et al.*, Scavenger receptor CD36 mediates inhibition of cholesterol synthesis via activation of the PPARγ/PGC-1α pathway and Insig1/2 expression in hepatocytes. *Faseb j* **28**, 1910-1923 (2014).
34. W. Tang *et al.*, Adenylyl cyclase 1 as a major isoform to generate cAMP signaling for apoA-1-mediated cholesterol efflux pathway. *J Lipid Res* **59**, 635-645 (2018).
35. W. Y. Hsieh *et al.*, Toll-Like Receptors Induce Signal-Specific Reprogramming of the Macrophage Lipidome. *Cell Metab* **32**, 128-143.e125 (2020).
36. M. Bedard *et al.*, A terpene nucleoside from M. tuberculosis induces lysosomal lipid storage in foamy macrophages. *J Clin Invest* **133** (2023).
37. P. E. Almeida *et al.*, Mycobacterium bovis bacillus Calmette-Guerin infection induces TLR2-dependent peroxisome proliferator-activated receptor gamma expression and activation: functions in inflammation, lipid metabolism, and pathogenesis. *J Immunol* **183**, 1337-1345 (2009).
38. A. C. Li, C. K. Glass, The macrophage foam cell as a target for therapeutic intervention. *Nat Med* **8**, 1235-1242 (2002).
39. M. Eom, K. L. Hudkins, C. E. Alpers, Foam cells and the pathogenesis of kidney disease. *Curr Opin Nephrol Hypertens* **24**, 245-251 (2015).
40. T. Fuchs *et al.*, Expression of combinatorial immunoglobulins in macrophages in the tumor microenvironment. *PLoS One* **13**, e0204108 (2018).

483 **Main Figure Legends**

484 **Fig. 1. Spatial distribution of foam cells and storage lipids in *C. neoformans*-infected**
485 **murine lungs**. **A-B.** H&E staining of formalin-fixed, paraffin-embedded lung sections from *C.*
486 *neoformans* H99-infected mice. Images were photographed at (A) 100x magnification; scale bar
487 is 100 μm; and (B) 400x magnification; scale bar is 10 μm. Black arrows indicate foam cells. **C.**
488 MALDI imaging of representative CE and TAG species in infected lung sections. The left panel
489 shows H&E staining of infected tissue sections (scale bar is 2 mm). The yellow lines delineate
490 areas enriched in fungal cells (Crypto-rich), while the blue lines define areas enriched in foam
491 cells (FCell-rich). The three additional panels show MALDI imaging of storage lipids in lung
492 sections contiguous to those used for H&E staining. Representative species are shown: CE
493 (16:0) $[M+K]^+$ *m/z* 663.48 and TAG (46:0) $[M+K]^+$ *m/z* 817.669 signals tend to correspond to
494 cryptococci-enriched areas, while TAG (50:1) $[M+K]^+$ *m/z* 871.716 tends to be reduced in those
495 same areas. Areas delimited by white lines correspond to some cryptococci-enriched areas in
496 the H&E-stained section. Corresponding images of uninfected lung sections are shown in Fig.
497 S2. **D.** Quantification of CE and TAG MALDI imaging intensity (expressed as ion count).
498 Quantification of lipid species was performed in uninfected tissue and in fungus-rich (CN-R) and
499 foam-cell-rich (FC-R) areas of the infected tissue. Mean and SEM of 9 sections from three
500 uninfected animals (3 sections per animal) and 12 sections from four infected animals (3
501 sections per animal) are shown. **, $p < 0.05$; ****, $p < 0.001$ (unpaired *t*-test).

502 **Fig. 2. Characterization of lipid droplets induced by *C. neoformans* infection and**
503 **comparisons with *M. tuberculosis*-induced effects. A.** Lipid droplet content of MDM
504 determined by imaging flow cytometry. Representative images of MDM uninfected (leftmost
505 panel) and infected with mCherry-tagged *C. neoformans*. The two rightmost panels show
506 macrophages in the infected culture wells carrying and not carrying intracellular fungi (orange
507 fluorescence). Cells were stained with Bodipy 493/503 (neutral lipid dye, green fluorescence).
508 Images were acquired by imaging flow cytometry at 24 hrs post-infection. **B.** Quantification of
509 lipid droplet content by imaging flow cytometry expressed as median fluorescence intensity of
510 Bodipy 493/503. Each dot represents one human donor. **C.** Neutral lipid measurements in
511 MDM. TAG and cholesterol were measured in infected and uninfected cells using a
512 commercially available kit. The box plots show lower quartile, median, and upper quartile of the
513 distribution of multiple donors. The whiskers represent minimum and maximum values. The plus
514 symbol indicates the mean. ns, non-significant; *, $p < 0.05$ (paired *t*-test). Each dot represents
515 one human donor. **D.** Effect on lipid droplets of MDM treatment with A922500 (DGAT-1 inhibitor)

516 or rapamycin (mTORC1 inhibitor). MDM were infected with *C. neoformans* or with *M.*
517 *tuberculosis* for 24h with an MOI = 4 in both infections. DMSO (vehicle control) and each drug
518 were added for the duration of infection. Lipid droplet content was quantified by imaging flow
519 cytometry and expressed as Bodipy MFI, as described in panel A and in Fig. S3AB. Results are
520 shown as ratios of Bodipy MFI of drug-treated to vehicle-treated infected cells. Mean and SD
521 are shown. ns, non-significant; **, $p < 0.01$ (unpaired *t*-test). Each dot represents one human
522 donor. **E-F.** Pathway analysis of the transcriptomes of *M. tuberculosis*- and *C. neoformans*-
523 infected MDM. The two panels show Gene Ontology (GO) annotations related to metabolic
524 processes that were (**E**) downregulated in *M. tuberculosis*-infected MDM and (**F**) upregulated in
525 *C. neoformans*-infected MDM, relative to uninfected control cells. The differential expression
526 between sample classes (infected vs uninfected) was tested with coincident extreme ranks in
527 numerical observations (CERNO). Pathways were selected using a cutoff false discovery rate of
528 0.05; the *p*-values for these pathways are plotted onto the x-axis. To represent effect size,
529 pathway gene sets containing fewer genes were given greater bar height/font size than were
530 larger sets that yielded similar *p* values. For visualization purposes, top ranking annotations are
531 shown. Additional pathway analysis data are shown in *Supplementary Fig. S4*. **G.**
532 Cytokine/chemokine levels in MDM. MDM from five donors were infected with *C. neoformans*
533 (Crypto) or *M. tuberculosis* (TB), as in panel C. A Luminex platform was used to measure
534 cytokine/chemokine/growth factor concentration in the supernatants of uninfected (control) and
535 infected cells. Each sample was measured in duplicate. Average Z-score of 5 donors was
536 calculated for each analyte (gradient from green to red represents increasing concentrations).
537 White asterisks indicate significant differences between uninfected and infected cells. *, $p <$
538 0.05; **, $p < 0.01$; ***, $p < 0.001$ (paired *t*-test).

539 **Fig. 3. Spatial distribution of foam cells and storage lipids in papillary renal cell**
540 **carcinoma (pRCC). A-B.** MALDI imaging of representative CE and TAG species in pRCC
541 resected tissues. MALDI-2 MSI ion distribution for CE 16:1 $[M+K]^+$ *m/z* 661.532 (panel A) and
542 TAG 52:2 $[M+K]^+$ *m/z* 897.731 (panel B) are shown in frozen pRCC tissue sections; scale bar
543 is 3 mm. The white rectangles delineate areas of high signal intensity that are magnified in the
544 corresponding histology panels C-D. **C-H.** H&E staining of frozen pRCC tissue sections. Serial
545 sections to those used for MALDI imaging were H&E stained. Each column corresponds to the
546 top MALDI image (left panels, CE 16:1; right panels, TAG 52:2). The black box in each row
547 marks the area of tissue shown at higher magnification in the corresponding panel below. **C-D**.
548 scale bar is 500 mm. Black arrows in panel C mark large foam cell aggregates. The black box in

C marks an area enriched for foam cell aggregates, which are further magnified in panel E. The black box in D marks an area enriched for foam cells interspersed among tumor cells, which is further magnified in panel F. **E-F.** scale bar is 150 mm. The black boxes in these panels mark areas further magnified in panels G and H, respectively. **G-H.** scale bar is 50 mm. Panel G shows a foam cell aggregate; panel H shows foam cells interspersed among tumor cells.

Fig. 4. Characterization of the lipogenic effects of treatment of human primary macrophages with conditioned medium from ACHN cell cultures. Monocyte-derived macrophages (MDM) were incubated with ACHN-conditioned medium; lipid droplet and neutral lipid content was measured after 7 days of treatment. **A.** Lipid droplet content of MDM determined by imaging flow cytometry. Representative images of MDM untreated and ACHN-treated stained with Bodipy 493/503 (neutral lipid dye, green fluorescence) acquired by imaging flow cytometry. **B.** Quantification of lipid droplet content by imaging flow cytometry expressed as median fluorescence intensity (MFI) of Bodipy 493/503. Each dot represents one human donor. **C.** Neutral lipid measurements in MDM. TAG and cholesterol were measured in infected and uninfected cells using a commercially available kit. The box plots show lower quartile, median, and upper quartile of the distribution of multiple donors. The whiskers represent minimum and maximum values. The plus symbol indicates the mean. *, $p < 0.05$; **, $p < 0.01$ (Wilcoxon signed-rank test). **D.** Pathway analysis of the transcriptome of ACHN-medium-treated MDM. The panel shows Gene Ontology (GO) annotations related to metabolic processes that were upregulated in ACHN-medium-treated MDM, relative to untreated control cells. The differential expression between sample classes (infected vs uninfected) was tested with coincident extreme ranks in numerical observations (CERNO). Pathways were selected using a cutoff false discovery rate of 0.055; the *p*-values for these pathways are plotted onto the x-axis. To represent effect size, pathway gene sets containing fewer genes were given greater bar height/font size than were larger sets that yielded similar *p* values. It is noted that immunoglobulin production by macrophages in the context of tumor microenvironments has been described (40) - it is not discussed as it does not appear relevant to the topic of our report. Additional pathway analysis data are shown in *Supplementary Fig. S9*.

Figure 1

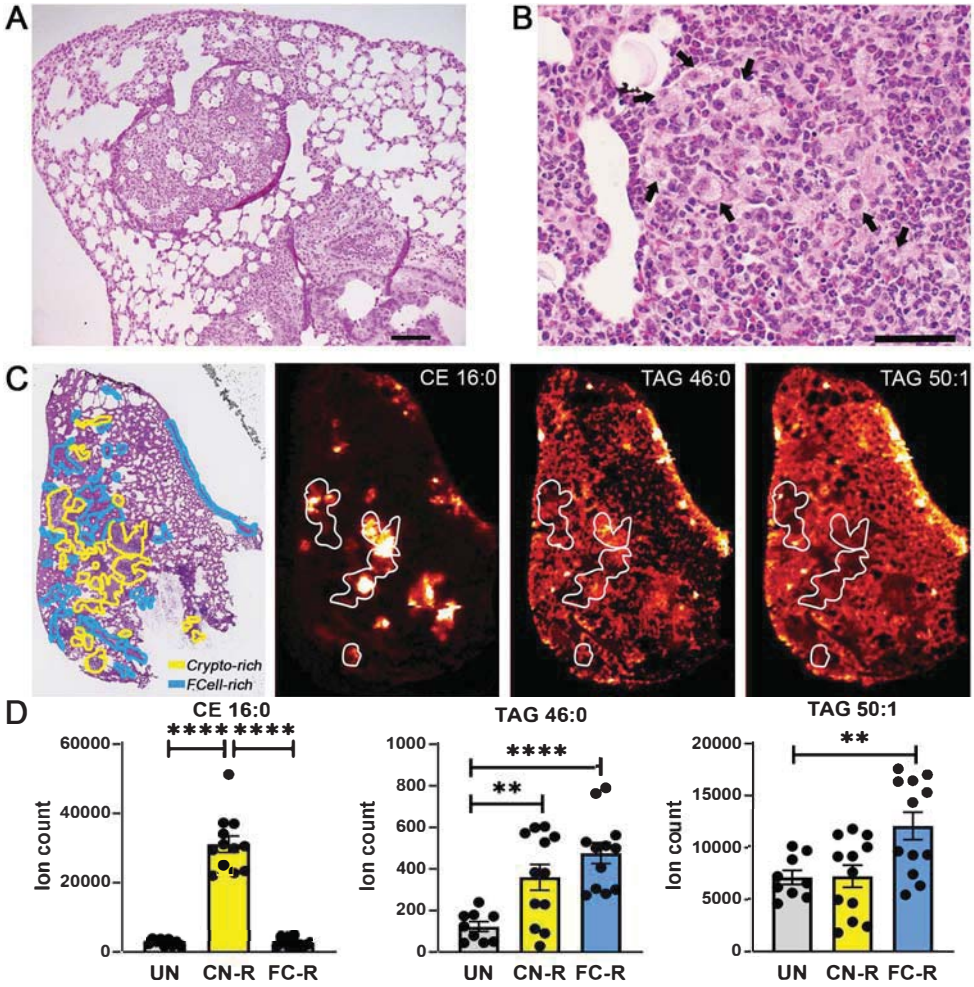
A
B
C
CE 16:0
TAG 46:0
TAG 50:1
Crypto-rich
F.Cell-rich
D
CE 16:0
TAG 46:0
TAG 50:1
Ion count
UN
CN-R
FC-R
****
**

Figure 2

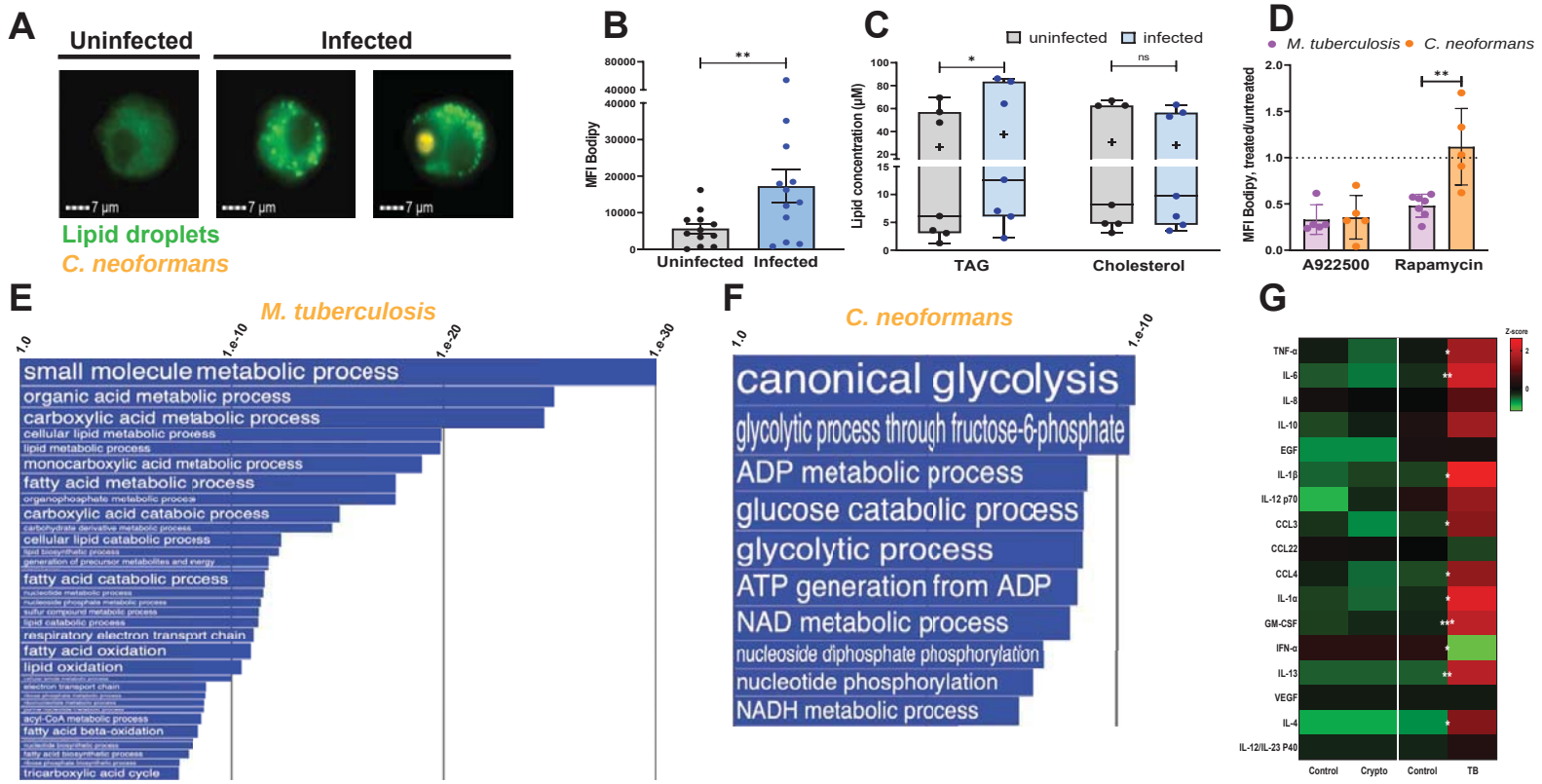
A
Uninfected
Infected
7 µm
7 µm
7 µm
Lipid droplets
C. neoformans
B
MFI Bodipy
Uninfected
Infected
C
uninfected
infected
Lipid concentration (µM)
TAG
Cholesterol
D
M. tuberculosis
C. neoformans
MFI Bodipy, treated/untreated
A922500
Rapamycin
E
M. tuberculosis
small molecule metabolic process
organic acid metabolic process
carboxylic acid metabolic process
cellular lipid metabolic process
lipid metabolic process
monocarboxylic acid metabolic process
fatty acid metabolic process
carboxylic acid catabolic process
cellular lipid catabolic process
fatty acid catabolic process
respiratory electron transport chain
fatty acid oxidation
lipid oxidation
electron transport chain
acyl-CoA metabolic process
fatty acid beta-oxidation
tricarboxylic acid cycle
F
C. neoformans
canonical glycolysis
glycolytic process through fructose-6-phosphate
ADP metabolic process
glucose catabolic process
glycolytic process
ATP generation from ADP
NAD metabolic process
nucleoside diphosphate phosphorylation
nucleotide phosphorylation
NADH metabolic process
G
Z-score
TNF-α
IL-6
IL-8
IL-10
EGF
IL-1β
IL-12 p70
CCL3
CCL22
CCL4
IL-1α
GM-CSF
IFN-α
IL-13
VEGF
IL-4
IL-12/IL-23 P40
Control
Crypto
Control
TB

Figure 3

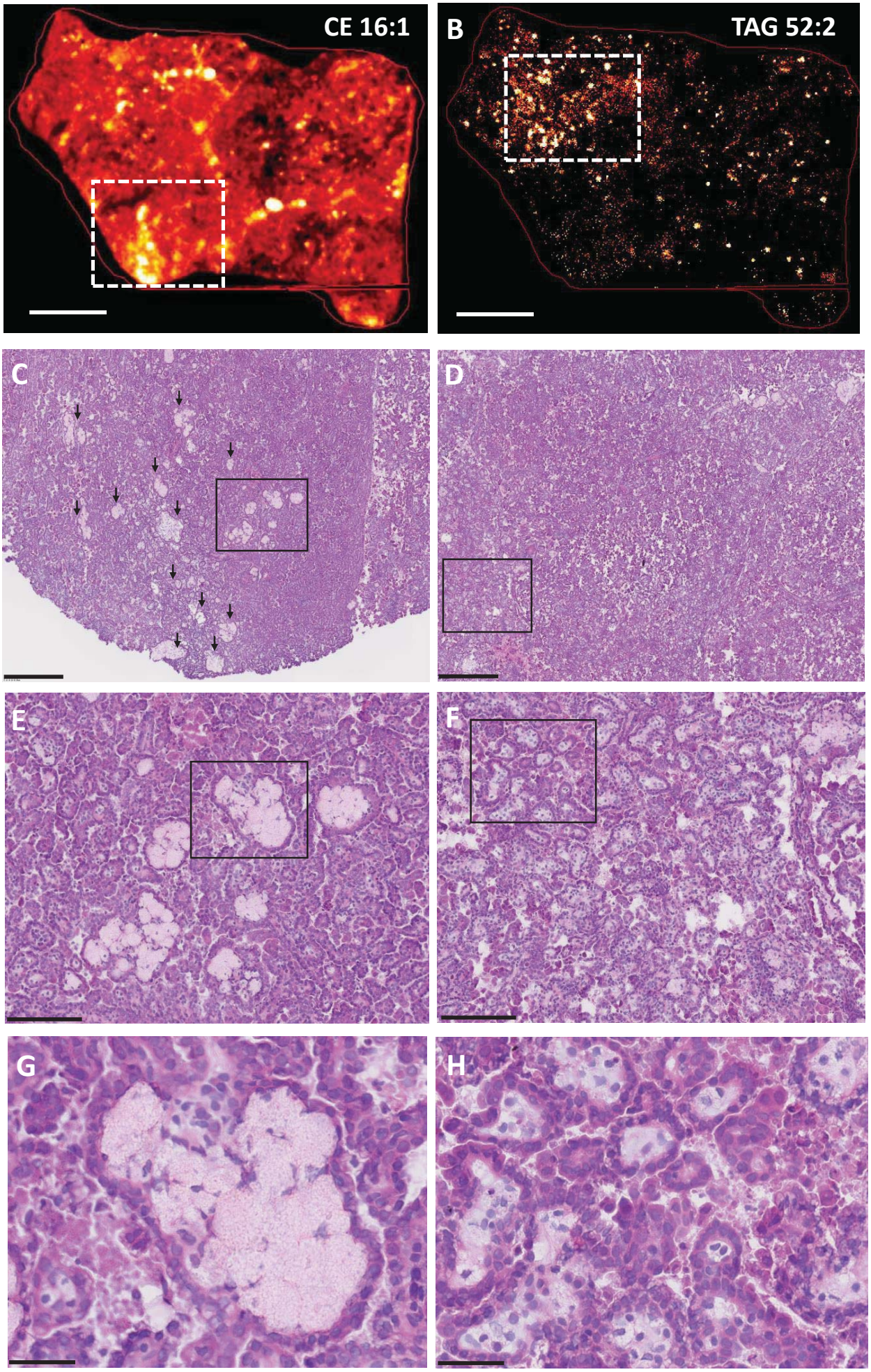

Figure 4

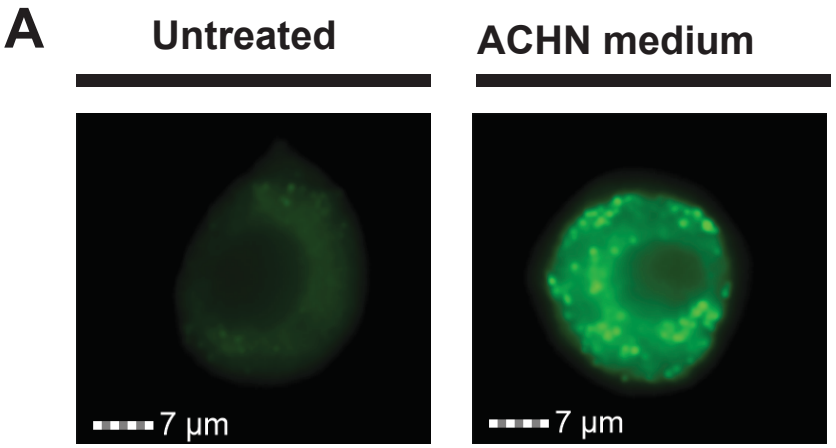
A
Untreated
ACHN medium
7 µm
7 µm

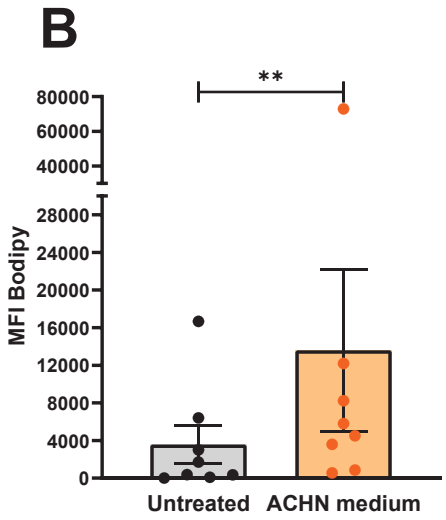
B
**
MFI Bodipy
80000
60000
40000
28000
24000
20000
16000
12000
8000
4000
0
Untreated
ACHN medium

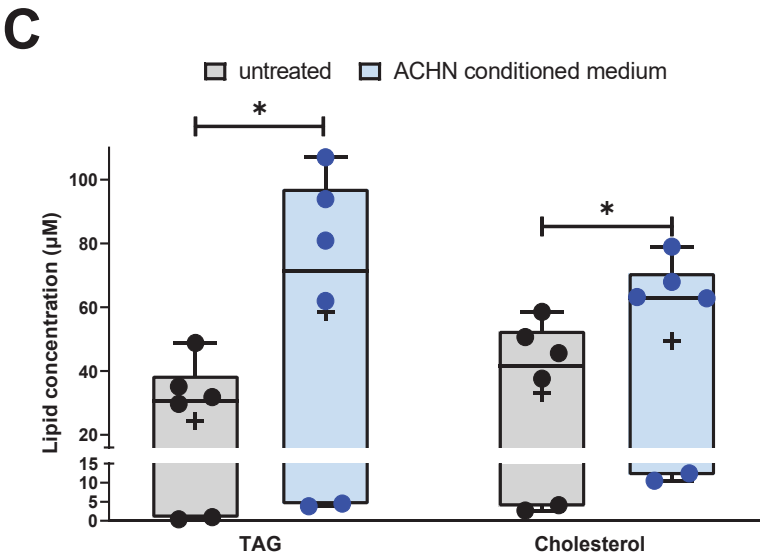
C
untreated
ACHN conditioned medium
*
*
Lipid concentration (µM)
100
80
60
40
20
15
10
5
0
TAG
Cholesterol

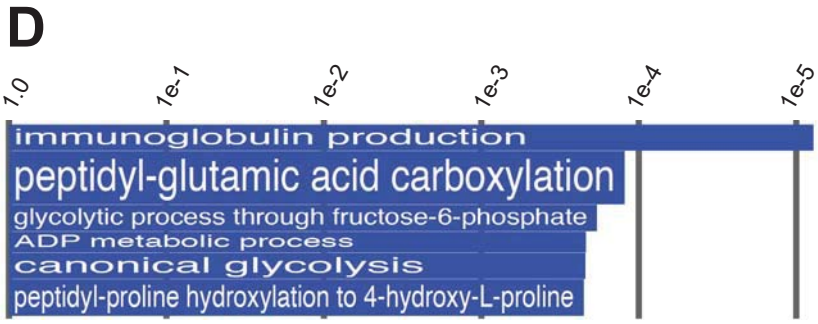
D
1.0
1e-1
1e-2
1e-3
1e-4
1e-5
immunoglobulin production
peptidyl-glutamic acid carboxylation
glycolytic process through fructose-6-phosphate
ADP metabolic process
canonical glycolysis
peptidyl-proline hydroxylation to 4-hydroxy-L-proline